Non-destructive detection of highway hidden layer defects using a ground-penetrating radar and adaptive particle swarm support vector machine

Xinyu Liu [Corresp., 1, 2, 3] , **Peiwen Hao** [1] , **Aihui Wang** [4] , **Liangqi Zhang** [2] , **Bo Gu** [3] , **Xinyan Lu** [3]

[1] CHANG'AN University, Xian, China

[2] Henan Wanli Rord&Bridge Group Co. Ltd., Xuchang, China

[3] School of Electric Power, North China University of Water Resource and Electric Power, Zhengzhou, China

[4] Zhongyuan University of Technology, Zhengzhou, China

Corresponding Author: Xinyu Liu
Email address: lxy@ncwu.edu.cn

In this paper, a method that uses a ground-penetrating radar (GPR) and the adaptive particle swarm support vector machine (SVM) method is proposed for detecting and recognizing hidden layer defects in highways. Three common road features, namely cracks, voids, and subsidence, were collected using ground-penetrating imaging. Image segmentation was performed on acquired images. Original features were extracted from thresholded binary images and were compressed using the kl algorithm. The SVM classification algorithm was used for condition classification. For parameter optimization of the SVM algorithm, the grid search method and particle swarm optimization algorithm were used. The recognition rate using the grid search method was 88. 333%; the PSO approach often yielded local maxima, and the recognition rate was 86.667%; the improved adaptive PSO algorithm avoided local maxima and increased the recognition rate to 91.667%.

1 **Non-destructive detection of highway hidden layer**
2 **defects using a ground-penetrating radar and adaptive**
3 **particle swarm support vector machine**
4

6 Xinyu Liu [1,2,3], Peiwen Hao [1], Aihui Wang [4], Liangqi Zhang [3], Bo Gu [2] and Xinyan Lu [2]
7
8 [1] CHANG'AN University, Xian, China
9 [2] School of Electric Power, North China University of Water Resource and Electric Power,
10 Zhengzhou, China
11 [3] Henan Wanli Rord&Bridge Group Co. Ltd.Xuchang, China
12 [4] Zhongyuan University of Technology, Zhengzhou, China; a. wang@zut.edu.cn
13
14 Corresponding Author:
15 Xinyu Liu[1]
16 36 Beihuan Road, Zhengzhou, Henan Province, CO 450011, China
17 Email address: lxy@ncwu.edu.cn

19 ## Abstract

20 In this paper, a method that uses a ground-penetrating radar (GPR) and the adaptive particle
21 swarm support vector machine (SVM) method is proposed for detecting and recognizing hidden
22 layer defects in highways. Three common road features, namely cracks, voids, and subsidence,
23 were collected using ground-penetrating imaging. Image segmentation was performed on
24 acquired images. Original features were extracted from thresholded binary images and were
25 compressed using the kl algorithm. The SVM classification algorithm was used for condition
26 classification. For parameter optimization of the SVM algorithm, the grid search method and
27 particle swarm optimization algorithm were used. The recognition rate using the grid search
28 method was 88. 333%; the particle swarm optimization (PSO) approach often yielded local
29 maxima, and the recognition rate was 86.667%; the improved adaptive PSO algorithm avoided
30 local maxima and increased the recognition rate to 91.667%.

31 **Keywords:** 5 Ground penetrating radar (GPR); Image segmentation; Feature extraction; Support
32 vector machine (SVM); Grid search method; Particle swarm optimization (PSO)

33

34 ## Introduction

35 Many forms of road deterioration can develop after prolonged utilization of expressways;
36 examples include crack formation, development of voids, and subsidence [1]. The main cause of
37 these conditions is the appearance of cracks under the roadbed, which gradually affects the road

38   surface and causes surface cracks. Continued use of expressways causes incremental damage and
39   can significantly increase the amount and type of maintenance work. With increasing traffic
40   volumes in China, it is necessary to develop more efficient and automated road condition-
41   detection methods.

42   Much research has been conducted on using ground-penetrating radars (GPRs) for landform
43   surveys. With the continuous development of the GPR technology and with the improvement of
44   detection accuracy, the use of the GPR technology for non-destructive detection of structural
45   road conditions has been garnering increasing attention. Yuanlei et al. used the GPR technology
46   to detect different physical anomalies, based on physical simulations and field tests, and the
47   response characteristics across the two scenarios were consistent [2]. Shili et al. used the GPR
48   technology to detect hidden defects, such as road breaks, voids, and subsidence, and acquired
49   defect images [3]. Literature [4] uses amplitude attenuation method in ultrasonic testing to
50   evaluate the corrosion damage of reinforced structures in concrete roads. Document [5] detects
51   the defects in concrete road base by ultrasonic detection technology and establishes the
52   mathematical model of sound wave propagation in different media. Literature [6] establishes the
53   mathematical model of ultrasonic wave propagation in asphalt pavement and concrete pavement
54   to identify highway surface defects, analyzes its feasibility and realizes ultrasonic nondestructive
55   testing of road defects based on this.

56   Using methods from the image recognition field, this study focuses on the design of shallow
57   hidden defect classifiers based on the support vector machine (SVM) algorithm. The SVM
58   method has been widely studied and applied in different contexts. Hou improved the SVM
59   algorithm's low precision around the hyperplane and reduced its computational complexity for
60   processing large amounts of data; they also improved the algorithm's training efficiency, and
61   managed to reduce the number of false calls [7]. El-Saadawi used the SVM algorithm for the
62   stator winding protection of synchronous generators, and achieved good results [8]. The SVM
63   algorithm has been widely used in a variety of context, such as big data, medical, agricultural,
64   and transportation applications [9,10,11]. Using the SVM algorithm, this study optimizes and
65   improves its parameter selection process. By comparing the optimization performance of the grid
66   search (GS) [12] method and the particle swarm optimization (PSO) [13] algorithm, the
67   superiority of the PSO algorithm is demonstrated, and the SVM classification algorithm for PSO-
68   based parameter optimization is studied [14]. By collecting radar images of three diseases on the
69   107 national highway section from Zhengzhou to Xinxiang in Henan Province, it is shown that
70   the obtained method performs well in detecting hidden pavement defects.

71

Image preprocessing and feature extraction

73   *1. Detection principle of the ground penetrating radar*

74   In the GPR approach, the ground is irradiated by high-frequency electromagnetic waves using a
75   transmitting antenna, while the waves reflected from the ground are detected using a receiving

76 antenna. Electromagnetic waves are reflected differently from different underground media; thus,
77 different waveforms registered by the receiving computer for analysis [15]. Figure 1 shows the
78 GPR detection process.

79 The reflection coefficient of an electromagnetic wave mainly depends on the dielectric constants
80 of the medium in which the wave travels originally and the medium from which the wave is
81 reflected, as given by Equations 1 and 2:

$$r = \frac{\sqrt{\varepsilon_1} - \sqrt{\varepsilon_2}}{\sqrt{\varepsilon_1} + \sqrt{\varepsilon_2}}$$

(1)

$$v = \frac{c}{\sqrt{\varepsilon_1}}$$

(2)

82 Where, r is the reflection coefficient; ε_1 ε_2 are the relative dielectric constant of the incident
83 medium and the medium from which the wave is reflected, v is the echo speed, and c is the
84 speed of light in vacuum.

85 *2. Selection of the ground penetrating radar*

86 The ground penetrating radar used in this study is LTD-2100 ground penetrating radar system
87 developed by China Electronics Technology Group Corporation. The main components of the
88 system are 900MHz shielded antenna, data acquisition host, computer, data cable, etc.

89 *3. Image preprocessing*

90 The original images of roads detected by a GPR include the reflection characteristics of road
91 conditions and various types of clutter caused by environmental factors. The clutter distribution
92 is typically non-uniform, affecting the correct recognition and classification of road conditions.
93 To improve the accuracy of the road condition determination, it is necessary to remove the effect
94 of this clutter [16]. To extract the features associated with various road conditions, the acquired
95 images should be segmented.

96 1) Image filtering

97 The objective of image filtering is to minimize the effects of noise and interference in raw
98 images. The noise and interference are mainly attributed to the processes – image acquisition and
99 image transmission. Gaussian filtering is typically used for image denoising, which can remove
100 unnecessary interference and protect the edge of the image.

101 2) Image segmentation

102 The objectives of image segmentation are to classify foreground and background pixels, and to
103 determine the organization of foreground pixels (i.e., detect foreground objects) [17].

104   The Canny operator has been widely used for image segmentation of radar images, and its
105   segmentation performance after Gaussian filtering is demonstrated in Figure 2. Fig. 2 (A) is the
106   original radar acquisition diagram. Fig. 2 (B) is the result after Gaussian transformation. It can be
107   seen that the clutter in the original image is removed. Fig. 2 (C) is the disease characteristic
108   waveform diagram extracted after Canny operator. To retain only the necessary information, the
109   image was subjected to the morphological operations of expansion and corrosion; the results are
110   shown in Figure 3. Figure 3 (A) is the image after Canny operator segmented the disease
111   waveform. Figure 3 (B) is an enhanced disease waveform diagram after the segmented waveform
112   is processed by digital morphology, so as to facilitate the extraction of disease features in the
113   following text. The processed image was segmented and objects were extracted using the vertical
114   projection method, as shown in Figure 4.

115   3) Feature extraction

116   Feature extraction should satisfy the following requirements: 1) features should have strong anti-
117   interference ability; 2) features should be insensitive to translation, rotation, and scale
118   transformation of images; 3) features should be insensitive to geometric distortions; 4) distance
119   between similar images should be as small as possible; and 5) distance between different images
120   should be as large as possible. The algorithm for extracting feature vectors should be simple, and
121   the dimensionality of the feature space should not be too high for ensuring the classification
122   performance of the system [18]. To satisfy the above requirements, the following features were
123   used: area, image complexity, image texture, and seven rectangular features.

124   In this study, three types of road hazards are studied, namely, road cracking, hollowing, and
125   subsidence. Through simulation and actual images, combined with the classification of expert
126   experience, three types of samples are collected to describe these conditions. Twentynine feature
127   vectors were extracted for each sample, and the obtained set of features is shown in Table 1,
128   Table 2, Table 3.

129   The dimensions of the different features are very different. Direct use of feature data not only
130   reduces the system performance, but also affects the classification accuracy. To avoid this
131   shortcoming, it is necessary to perform data normalization [19]. Let the eigenvector of a pattern
132   vector be $X = (x_1, x_2, ... x_m)$. Then the normalized eigenvector x_i' is

$$x_{ij}' = 0.1 + \frac{0.8(x_{ij} - x_{i,\min})}{x_{i,\max} - x_{i,\min}} \quad (i = 1, 2, ..., m) \tag{3}$$

133   Where, $x_{i,\max}, x_{i,\min}$ are the maximum and minimum of $\{x_i(k) | k - 1, ..., P\}$, and P is the overall
134   number of samples in the training set.

135   4) Feature selection

136   In this study, $K\text{-}L$ transformation was used as the feature selection algorithm [20]. $K\text{-}L$
137   transformation can take into account different classification information and realize supervised

138   feature extraction. Under the criterion of minimum mean square error, it can obtain an

139   orthogonal transformation matrix A that can map the original feature $\overset{\shortmid}{X}$ from high-dimensional

140   space D to low-dimensional space vector $\overset{\shortmid}{y}$. K-L transformation can retain the data component

141   with the largest variance in the original data and highlight the data difference. Empirical

142   knowledge was used for removing several highly correlated features, and K-L changes were

143   used for reducing the dimensionality of the original feature space. A relatively simple class-

144   center classifier was used for identifying the samples after the K-L dimensionality reduction

145   transformation. The recognition rate is shown in Figure 5 for the test set.

146   According to Figure 5, when the dimensionality of the feature space reaches 12, the

147   recognition rate saturates; thus, the optimal dimensionality of the feature space is 12. K-L

148   transformation can take into account different classification information, realize supervised

149   extraction of features with too high correlation, and then use K-L transformation to extract

150   data information from them, thus achieving the purpose of compressing dimensions and

151   improving recognition rate.

152

153   ## The SVM classifier design

154   *1. Basic principle of the SVM*

155   SVM is a binary classification algorithm that is trained using the supervised learning paradigm.

156   The algorithm attempts to determine an optimal classification hyperplane, whereby the edge

157   distance between two sample classes and the dividing hyperplane (decision boundary) is

158   maximized. The larger the edge distance is, the more separated the two sample classes are, the

159   stronger the classification robustness, and the better the method's generalizability [21]. The

160   hyperplane equation is

$$\omega^T x + b = 0 \qquad (4)$$

161   Where ω is the normal to the hyperplane, and x determines the angle with the hyperplane; b is

162   the distance between the hyperplane and the origin. The hyperplane is denoted as (ω, b); then,

163   the distance from a certain point (sample) to the hyperplane (ω, b) is denoted by r:

$$r = \frac{\left|\omega^T x + b\right|}{\|\omega\|} \qquad (5)$$

164   Let the support vector be 1 and point away from the hyperplane, so that $\left|\omega^T x + b\right| = 1$, and let the

165   vectors in the two different classes be γ and point away from the hyperplane:

$$\gamma = \frac{2}{\|\omega\|} \tag{6}$$

166   For optimal segmentation, we need to find the hyperplane with the largest interval; that is, we

167   need to find the parameters ω and b that maximize γ. According to equation (6), only $\|\omega\|^{-1}$

168   should be maximized.

169   *2. Optimization of the SVM classifier parameters*

170   We used MATLAB (Mathworks, Inc.) to validate the diagnostic accuracy of the SVM-based

171   classifier with respect to the road conditions. We obtained a dataset comprising 100 examples of

172   road cracking, hollowing, and subsidence conditions; 80% of these images were used for training

173   the method, while the remaining 20% were used for testing the classifier.

174   The performance of any SVM classifier depends on the penalty factor and kernel function

175   parameters. The optimal parameter values are typically determined using the grid search

176   approach, which exhausts the set of possible parameter combinations to determine the optimal

177   combination.

178   The penalty term c and the kernal function parameters g were considered to grow exponentially

179   in the $[2^{-14}, 2^{14}]$ range; at the same time, the step between each cell on the grid was set to 0.5, that

180   is, the growth time-points were $2^{-14}, 2^{-13.5}, ..., 2^{14}$. As shown in Figure 6, the best classification

181   performance was obtained for $\log_2(c) = 7.60$, best $\log_2(g) = -6.60$.

182   As shown in the retrieval results above, the accuracy of $\log_2(c)$ between $[2^5, 2^{10}]$ and $\log_2(g)$

183   between $[2^{-10}, 2^{-4}]$ was relatively good; thus, the step was set to 0.2 in this range, and the

184   parameters were further optimized. The results are shown in Figure 7.

185   According to Figure 7, the best classification was obtained for best=7 and best=−5.2. These

186   optimal values were used as the SVM classifier parameters for validating its classification

187   performance; then, the accuracy of the classifier with these parameters was characterized. The

188   validation results are shown in Figure 8, and the final validation accuracy rate was 88.333%, the

189   image recognition time is t = 0.630s.

190   *3. Adaptive mutation particle swarm*

191   The results obtained using the grid search approach can meet the desired detection requirements,

192   but because the grid search approach only considers discrete combinations of parameters, the

193   optimal solution can be easily missed. At the same time, the grid search method is exhaustive,

194   and needs to consider all the possible cases; thus, this optimization approach is time-consuming.

195   To improve the accuracy and reduce the computation time, the PSO algorithm is proposed in this

196   section.

197   1) The PSO approach

198   PSO simulates a flock of birds, which are modeled as massless particles [22]. Each particle has
199   only two attributes: velocity v and position x. Velocity represents the speed of movement, and
200   position represents the direction of movement. Each particle searches for the optimal solution
201   separately in the search space, and records it as the current individual extreme value P; the
202   individual extreme values are shared among all the particles in the entire swarm, and the optimal
203   individual extreme value is determined as the current global optimal solution G of the entire
204   swarm of particles. All of the particles in the particle swarm adjust their speeds and positions
205   according to the current individual extremum P found by themselves and the current global
206   optimal solution G shared by the entire particle swarm. The underlying PSO process is relatively
207   simple, and can be divided into the following steps: 1. initializing the particle swarm; 2.
208   evaluating the particles, that is, calculating the fitness values; 3. searching for individual extrema
209   P; 4. searching for the global optimal solution G; 5. modifying the particles' speeds and
210   positions [23]. The update equations are:

$$
\begin{aligned}
v_{id}^{k+1} &= \omega v_{id}^{k} + c_1 \cdot rand(0,1) \cdot (p_{id}^{k} - x_{id}^{k}) \\
&\quad + c_2 \cdot rand(0,1) \cdot (p_{gd}^{k} - x_{id}^{k}) \\
x_{id}^{k+1} &= x_{id}^{k} + v_{id}^{k+1}
\end{aligned}
\tag{7}
$$

211   Where ω is the inertia factor, c_1 and c_2 are the acceleration constants, and rand(0,1) are random
212   numbers in the interval (0,1). p_{id} denotes d the dimension of the individual extreme value of
213   variable i . p_{gd} represents the dimensionality d of the global optimal solution. k represents the
214   current number of iterations.

215   The following parameter values were used: $c_1 = 2, c_2 = 2$, population size = 20, maximal number
216   of iterations= 200, and cross-validation fold $K = 5$. The fitness curve for the optimized SVM
217   classifier parameters is shown in Figure 9.

218   After iteration 15, the fitness reached its optimal value. At this point, the classifier accuracy was
219   89.197%, the best c was 0.7596, and the best g was 0.7674. Although the basic PSO algorithm
220   exhibits a good convergence speed and good optimization performance, it can prematurely
221   converge onto a locally optimal solution; as a result, the population will easily stagnate without
222   external pressure.

223   2) Variation improvement

224   To deal with the premature convergence problem, we utilized the concept of mutations that is
225   often used in genetic algorithms, and incorporated mutations into the PSO framework. For that,
226   we defined a trigger to allow particles to escape locally optimal solutions, thus ensuring a global
227   search [24]. The population fitness variance σ^2 was used for determining whether a local

228 maximum was reached in the iteration process. The population fitness variance σ^2 was defined
229 as follows:

$$\sigma^2 = \sum_{i=1}^{N} (\frac{f_i - f_{avg}}{f})^2 \tag{8}$$

230 In the above equation, N is the number of particles, f is the normalized calibration factor, f_i is
231 the fitness of the first particle, and f_{avg} is the average fitness. It can be seen that the larger the
232 value of σ^2, the more divergent the particle swarm; conversely, the smaller the population
233 fitness variance, the more convergent the particle swarm is. Values of σ^2 close to zero indicate
234 that the particle swarm is approaching the globally optimal solution or is converging onto a
235 locally optimal solution. To avoid premature trapping of the particle swarm in local optima, the
236 swarm is subjected to mutations:

$$x_i(k+1) = C \cdot rand(0,1) \cdot x_i(k) \tag{9}$$

237 In the above equation, C is a normally distributed random number in the $[0,1]$ interval and is the
238 variation factor; $rand(0,1)$ is a random number in the $[0,1]$ range; k is the number of iterations.
239 Mutations alter the particles' positions and thus allow to escape local optima [25].

240 The fitness curve of the improved adaptive mutation PSO algorithm for SVM-based parameter
241 optimization is shown in Figure 10. Evidently, the best fitness converges to a local maximum
242 after 17 generations. Mutations allow the particle swarm to escape this local maximum after 97
243 generations; after that, optimization parameters are determined with higher accuracy. The finally
244 estimated parameter values are: $c = 7.751$, $g = 5.754$. The fitness at this global optimum is
245 91.698%.

246 3) Simulation results

247 Based on the results in the previous section, the SVM model was constructed using the following
248 parameter values: $c = 0.7596$ and $g = 0.7674$, which were determined using the PSO method.
249 The results are shown in Figure 11.

250 For these parameter values, the accuracy of the model was 86.667%, the image recognition time
251 is t = 0.590s; however, the recognition accuracy had not improved. The main explanation was the
252 trapping of the particle swarm in a local optimum during the process of parameter optimization.
253 An SVM classifier was then constructed and validated using $c = 7.751$ and $g = 5.754$; these
254 parameter values were determined using the adaptive mutation PSO algorithm. The validation
255 results are shown in Figure 12.

256 From Figure 12, the classification accuracy of the SVM classification model with the parameter
257 values determined by the adaptive mutation PSO was 91.667%, the image recognition time is t =

258   0.615s. This classification accuracy is significantly higher compared with that achieved by the
259   SVM method that uses parameters optimized by the grid search approach.

260

261   **Conclusions**

262   According to the requirements of automatic recognition of highway hidden layer conditions,
263   this paper proposes an automatic detection and recognition method that uses an SVM with
264   parameters optimized using the adaptive mutation PSO approach. In this method, PSO with
265   mutations is used for parameter optimization. In this study, three different methods were used for
266   parameter optimization: 1) the grid search method, 2) the PSO approach, and 3) the adaptive
267   mutation PSO. MATLAB and Python were used for implementing these optimization methods,
268   and the optimization processes and their results were validated. Compared with the grid search
269   method and the simple PSO approach, the accuracy of the SVM with parameters optimized using
270   mutation PSO was higher, translating into better performance on automatic identification of
271   highway conditions. Our simulation results showed that the classification accuracy of the SVM
272   classifier with the grid search method was 88.333%, the classification accuracy of the SVM
273   classifier with PSO was 86.667%, and the classification accuracy of the SVM classifier with
274   mutation PSO was 91.667%. Thus, the effect of SVM classifier with mutation PSO is obviously
275   better than that of the other two. Compared with the grid search method, the classification
276   accuracy was improved. However, owing to the pre-processing of images and processing of
277   feature-related data, some defect-related information is likely to become distorted, which can
278   affect the accuracy of recognition. If a zero-distortion image processing method can be found,
279   the recognition accuracy will be greatly improved. At present, only cracks, voids and subsidence
280   can be analyzed and studied, while asphalt pavement diseases and defects can be divided into 11
281   categories and 21 items. In order to better improve the scope of the identification system, further
282   research should be done on other types of defects.

283

284   **References**

285   1. Marecos V, Solla M, Fontul S, Antunes V. Assessing the pavement subgrade by combining
286   different non-destructive methods. Construction and Building Materials, 2017, 135:76-85.

287   2. Yuan-lei SI, Guo-lin W. Study on the response characteristics of different physical anomalies
288   in the detection of ground-penetrating radar. Journal of Yunnan University (Natural Sciences
289   Edition), 2018, 40(05):903-908.

290   3. Shi-li GUO, Lei XU. LI, Xiu-zhong. Application of GPR in detection of road surface
291   settlement. Progress in Geophysics, 2018, 33(03):1213-1217.

292   4. Ming-Te Liang,Po-Jen Su.Detection of the corrosion damage of rebar in concrete using
293   impact-echo method Cem Concr Res,31(2001), pp.1427-1436.

294 5. Tirupan Mandal,James M.Tinjum,Tuncer B.Edil.Non-destructive testing of cementitiously
295 stabilized materials using ultrasonic pulse velocity test[J]. Transportation Geotechnics, 2016, 6:
296 97-107.

297 6. Wen, M. Balasingam, T. Edil, J. Tinjum, A. Gokce, J. Wang,et alCharacterization of
298 cementitiously stabilized layers for use in pavement design and analysis Project 04–36 Test
299 Procedure Evaluation Report National Cooperative Highway Research Program,
300 Washington,D.C. (2011)

301 7. Hou K, Shao G, Wang H, et al. Research on practical power system stability analysis
302 algorithm based on modified SVM. Protection and Control of Modern Power Systems, 2018,
303 3(1):1-7.

304 8. El-Saadawi M, Hatata A. A novel protection scheme for synchronous generator stator
305 windings based on SVM. Protection and Control of Modern Power Systems, 2017, 2(1):24.

306 9. Wang W, Du X, Wang N. Building a cloud IDS using an efficient feature selection method
307 and SVM. IEEE Access, 2019, 7:1345-1354.

308 10. Wang C, Zhang Y, Song J, et al. A novel optimized SVM algorithm based on PSO with
309 saturation and mixed time-delays for classification of oil pipeline leak detection. Systems
310 Science and Control Engineering, 2019, 7(1):75-88.

311 11. Hongtao Z, Yuxia HU, Hanping M. Image recognition and classification of the stored-grain
312 pests based on support vector machine. Journal of Agricultural Mechanization Research, 2008,
313 08:36-38.

314 12. Xiaosheng L, Zhibang Z. Parameter optimization of Support Vector Machine based on
315 improved grid search method. Journal of Jiangxi University of Science and Technology, 2019,
316 40(01):5-9.

317 13. Yang L, Zhichuan Z, Alin H, et al. Pulmonary nodule recognition based on multiple kernel
318 learning support vector machine-PSO. Computational and Mathematical Methods in Medicine,
319 2018, 2018:1-10.

320 14. Ziji M, Yanru D, Hongli L, et al. Method of forecasting non-equal interval track irregularity
321 based on improved grey model and PSO-SVM. IEEE Access, 2018, 06:34812-34818.

322 15. Benedetto A, Tosti F, Bianchini Ciampoli LB, D'Amico F. An overview of ground-
323 penetrating radar signal processing techniques for road inspections. Signal Processing, 2017,
324 132:201-209.

325 16. Bu F, Bu F. A high-order clustering algorithm based on dropout deep learning for
326 heterogeneous data in cyber-physical-social systems. IEEE Access, 2017, PP(99), 6:1-1.

327 17. Fengjun C, Chenghan W, Mengmeng GU, YANDong Z. Spruce image segmentation
328 algorithm based on fully convolutional networks. Transactions of the Chinese Society for
329 Agricultural Machinery, 2018, 49(12):188-194 + 210.

330   18. Zhiyun X, Hong LIU. Adaptive features fusion and fast recognition of potato typical disease
331   images. Transactions of the Chinese Society for Agricultural Machinery, 2017, 48(12):26-32.

332   19. Chowdhury SA, Stepanov EA, Danieli M, Riccardi G. Automatic classification of speech
333   overlaps: Feature representation and algorithms. Computer Speech and Language, 2019, 55:145-
334   167.

335   20. Jun N. A data reduction algorithm based on K-L feature compression for cloud computing.
336   Microelectronics and Computer, 2016, 33(02):125-129.

337   21. Yueting L, Xiaoxia L, Sixuan L. Imbalanced dataset classification algorithm based on
338   improved support vector machine. Journal of Shihezi University (Natural Science), 2018,
339   36(05):637-643.

340   22. Hsieh YZ, Su MC, Chen JH, et al. Developing a PSO-based projection algorithm for a
341   porosity detection system using X-ray CT images of permeable concrete. IEEE Access, 2018,
342   6:64406-64415.

343   23. Yang J, Wang X, Bauer P et al. Extended PSO Based Collaborative Searching for Robotic
344   Swarms With practical constraints. IEEE Access, 2019, 7:76328-76341.

345   24. Yifei T, Meng Z, Jingwei L, et al. Research on intelligent welding robot path optimization
346   based on GA and PSO algorithms. IEEE Access, 2018, 6:65397-65404.

347   25. Deng W, Yao R, Zhao H, et al. A novel intelligent diagnosis method using optimal LS-SVM
348   with improved PSO algorithm. Soft Computing, 2019, 23(7):2445-2462.

Gray level co-occurrence matrix characteristics of cracks, voids, and subsidence.

Defect type	crack			
GLCM	0°	45°	60°	90°
contrast	1.333	2.149	1.436	2.194
correlation	0.895	0.826	0.893	0.826
energy	0.724	0.708	0.728	0.702
homogeneity	0.988	0.962	0.972	0.967
Defect type	void			
GLCM	0°	45°	60°	90°
contrast	0.998	1.501	1.273	1.806
correlation	0.473	0.235	0.335	0.075
energy	0.644	0.594	0.626	0.579
homogeneity	0.891	0.865	0.886	0.849
Defect type	subsidence			
GLCM	0°	45°	60°	90°
contrast	3.813	6.486	5.447	5.924
correlation	0.414	0.019	0.164	0.104
energy	0.795	0.750	0.768	0.758
homogeneity	0.931	0.884	0.902	0.838

Differential statistical matrix characteristics of cracks, voids, and subsidence.

GLDS	mean	contrast	asm	ent
crack	0.048	289.831	0.916	0.261
void	0.141	660.909	0.589	2.186
subsidence	0.121	765.796	0.794	0.5202

Seventh order invariant moment feature.

seven-order Hu moment	crack	void	subsidence
Φ1	5.076	4.059	4.463
Φ2	10.591	8.547	9.925
Φ3	22.646	15.286	19.998
Φ4	22.974	15.286	22.229
Φ5	45.786	30.563	19.562
Φ6	28.343	19.562	28.508
Φ7	43.134	35.275	38.163

Figure 1

GPR detection process.
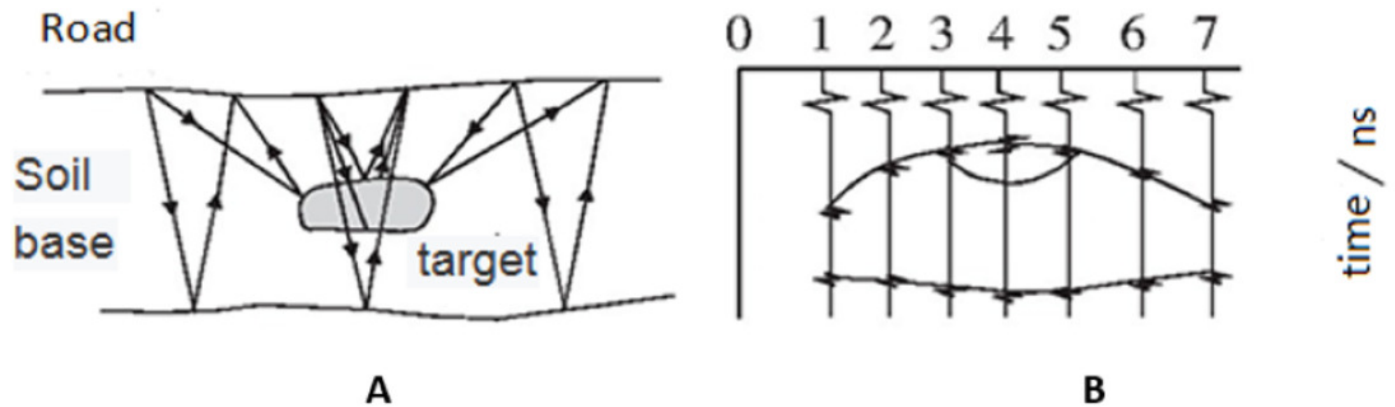
Figure 2

Image segmentation using the Canny operator.

(A) Original image. (B) Gauss filter image. (C) Canny operator processing.
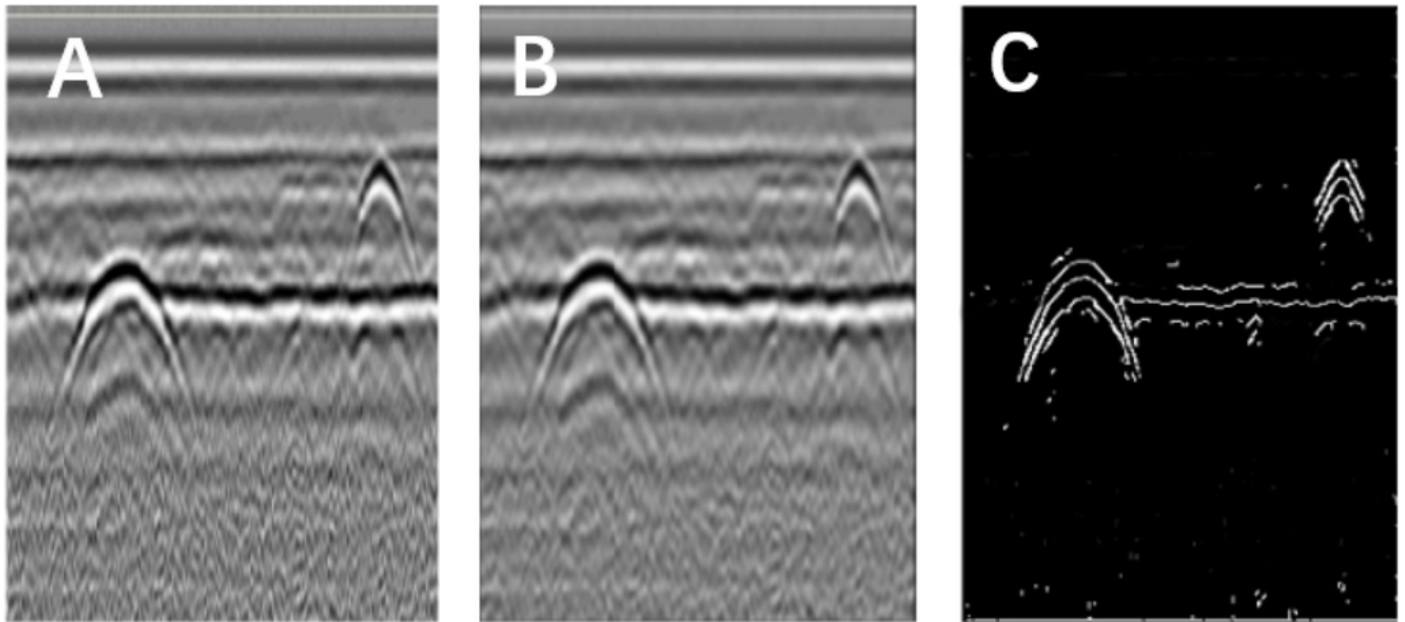
Figure 3

Morphological processing of digital images.

(**A**) Results obtained using the Canny operator. (**B**) Results obtained using morphological processing.
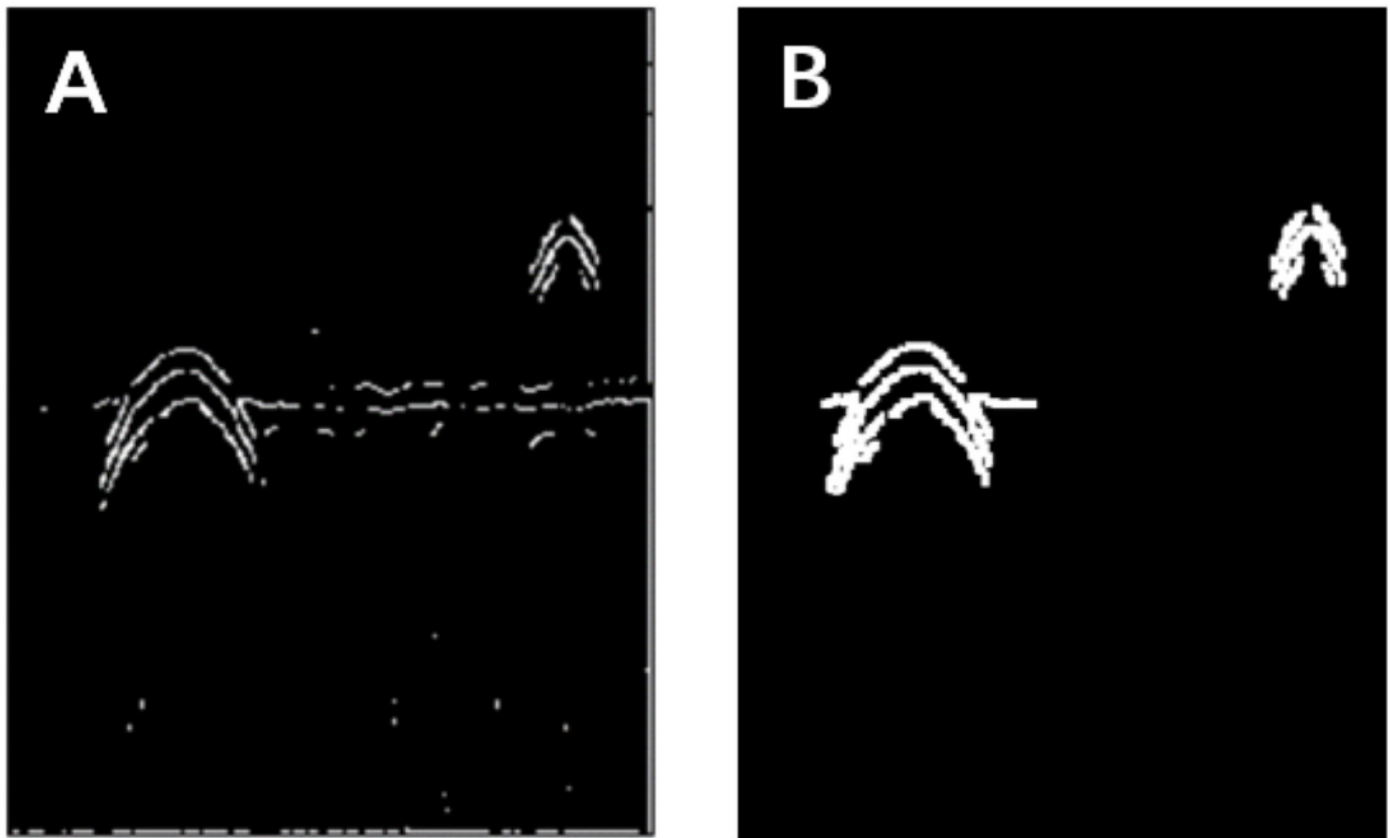
Figure 4

Projection segmentation results.
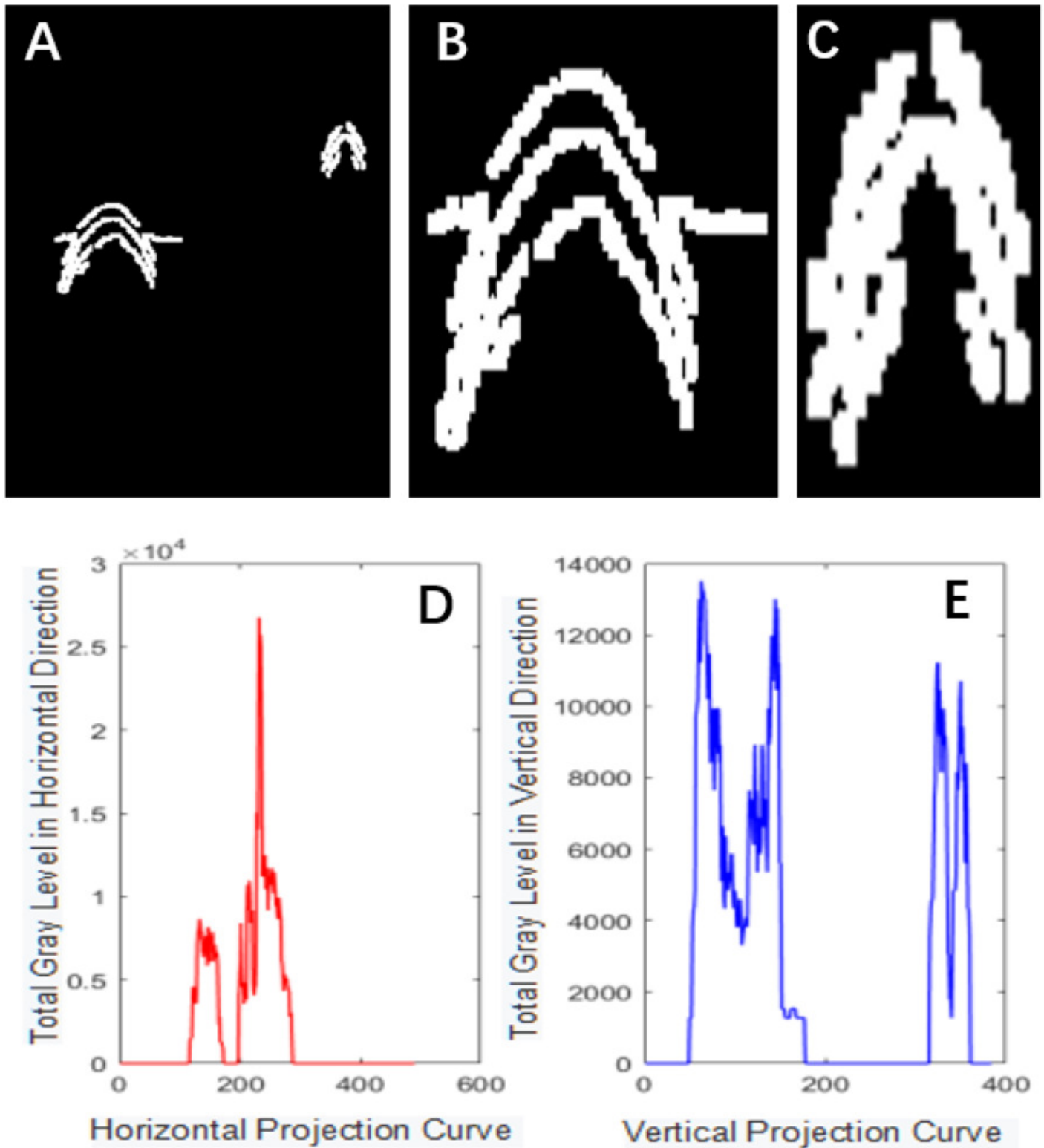
Figure 5

Dependence of the recognition rate on the number of features.
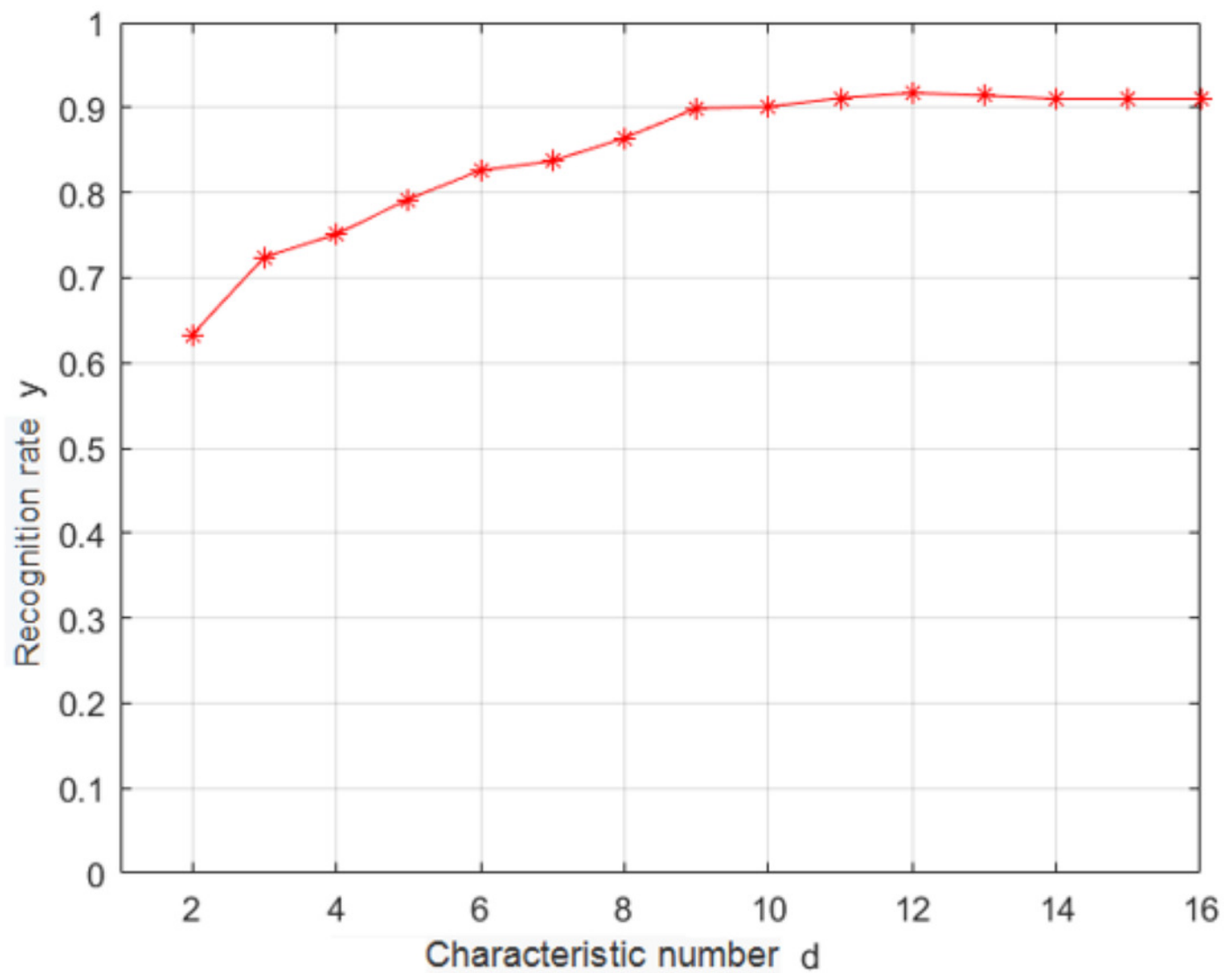
Figure 6

Parameter optimization results of the grid search method.
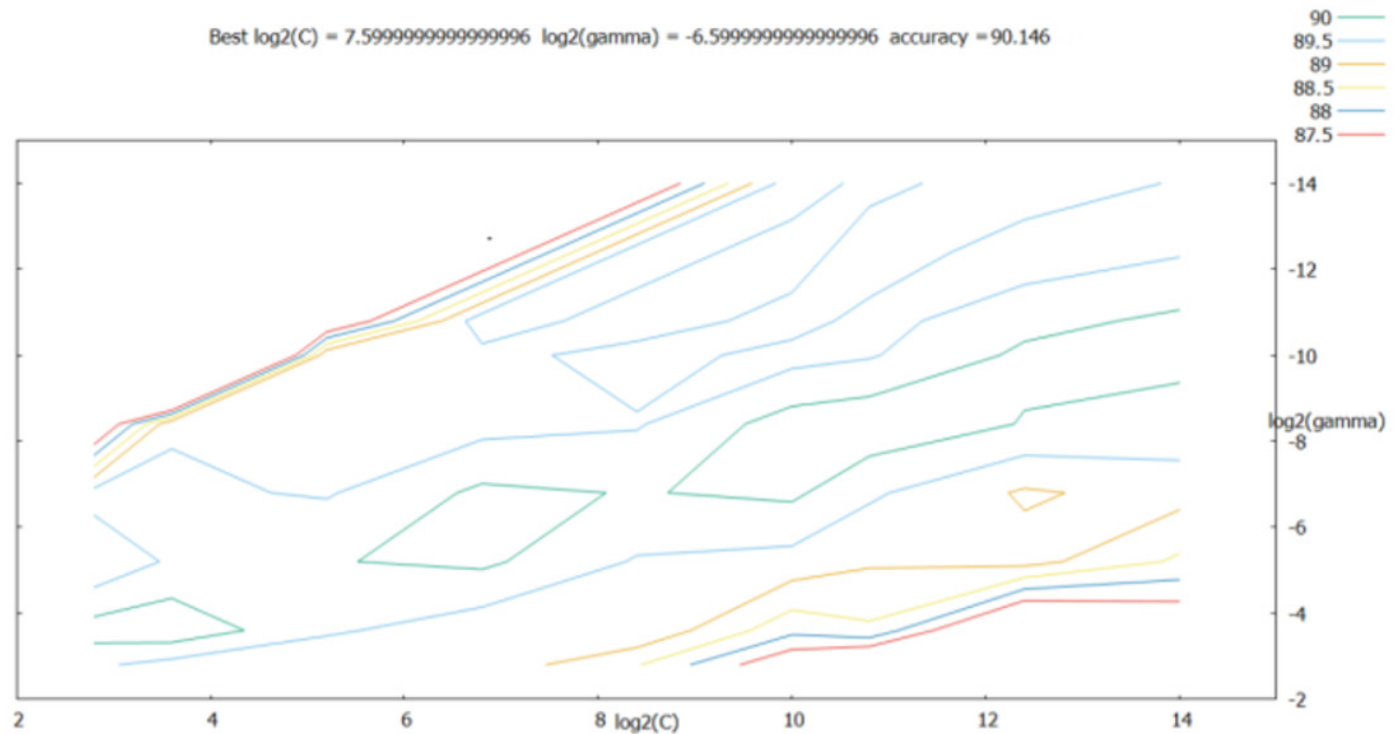
Figure 7

Results obtained after refining the step size.
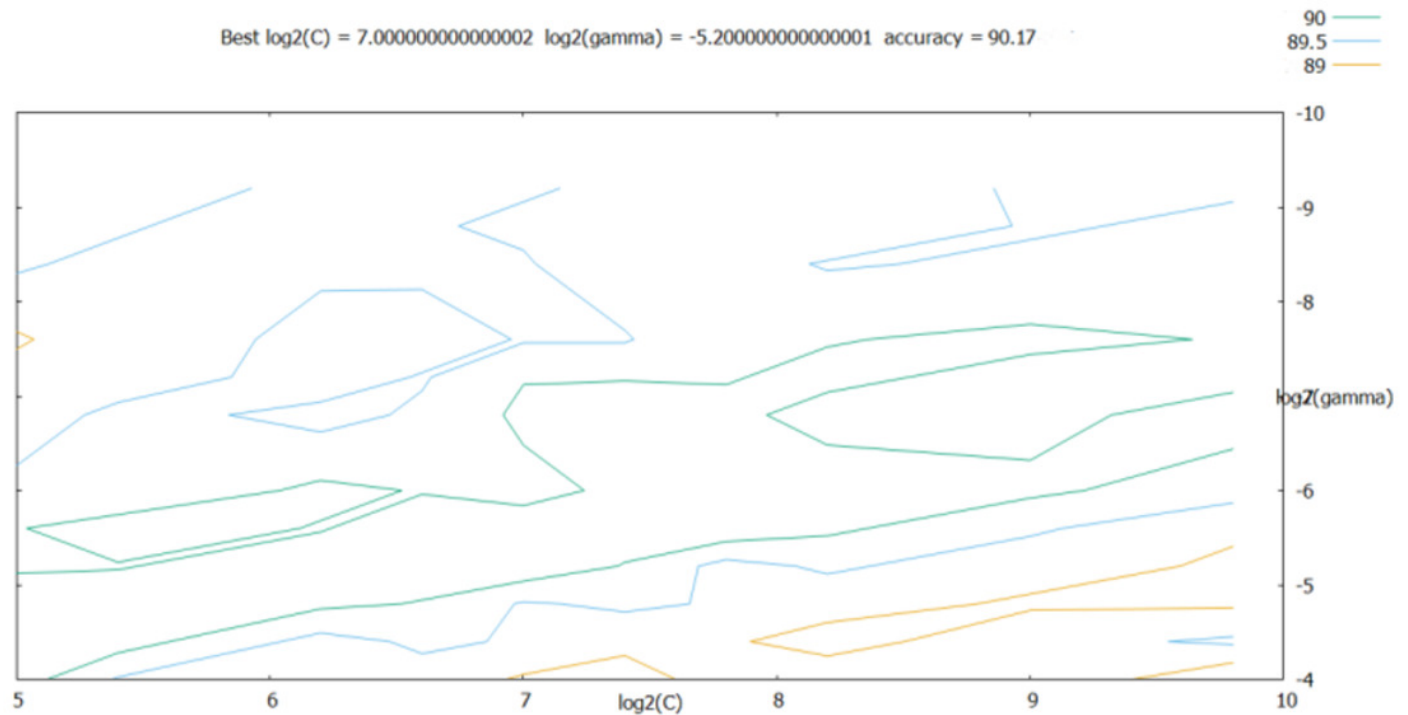
Figure 8

Test-set classification results after the grid search optimization of the SVM classifier parameters.
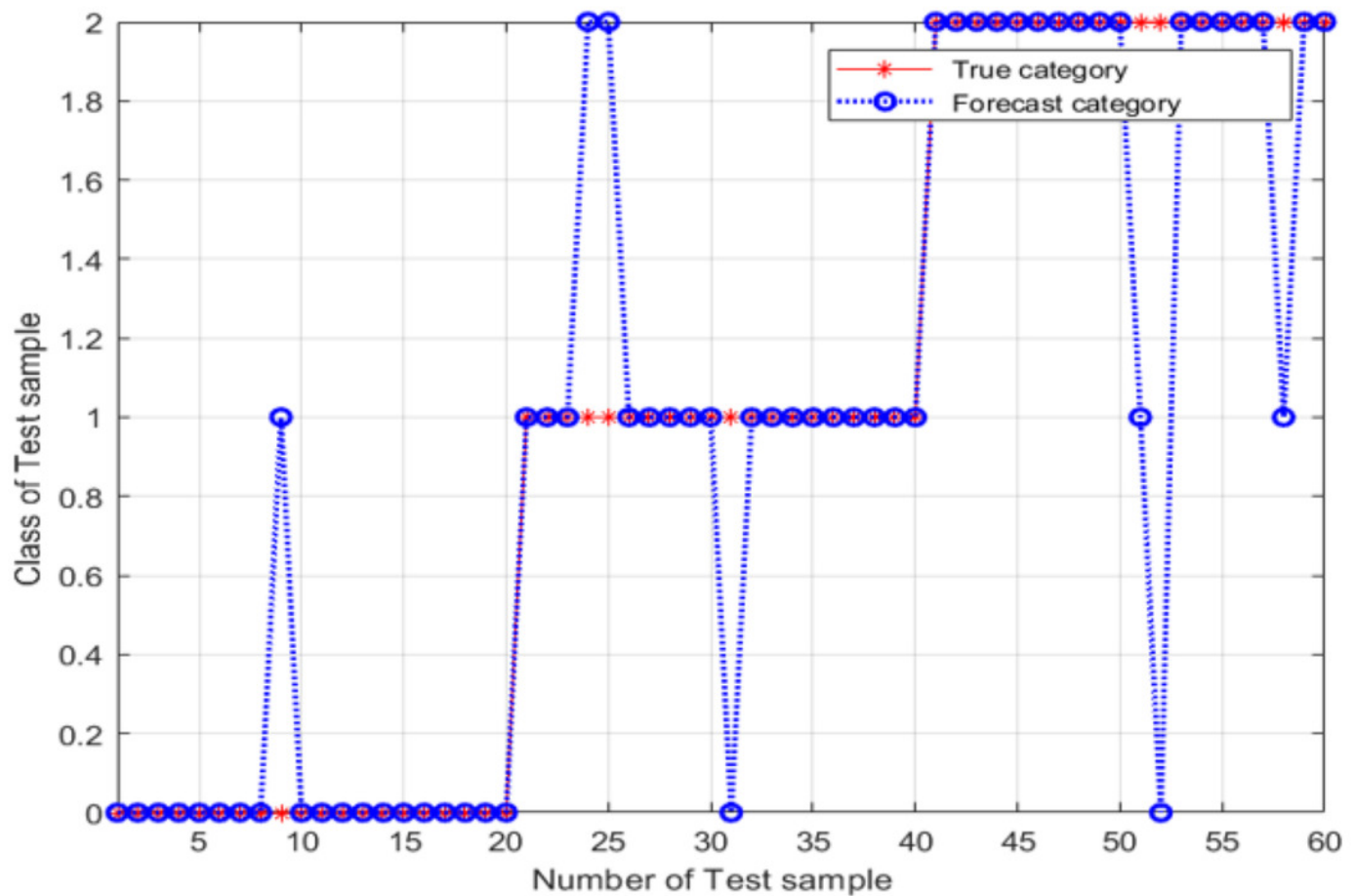
Figure 9

Fitness curve obtained after the PSO.
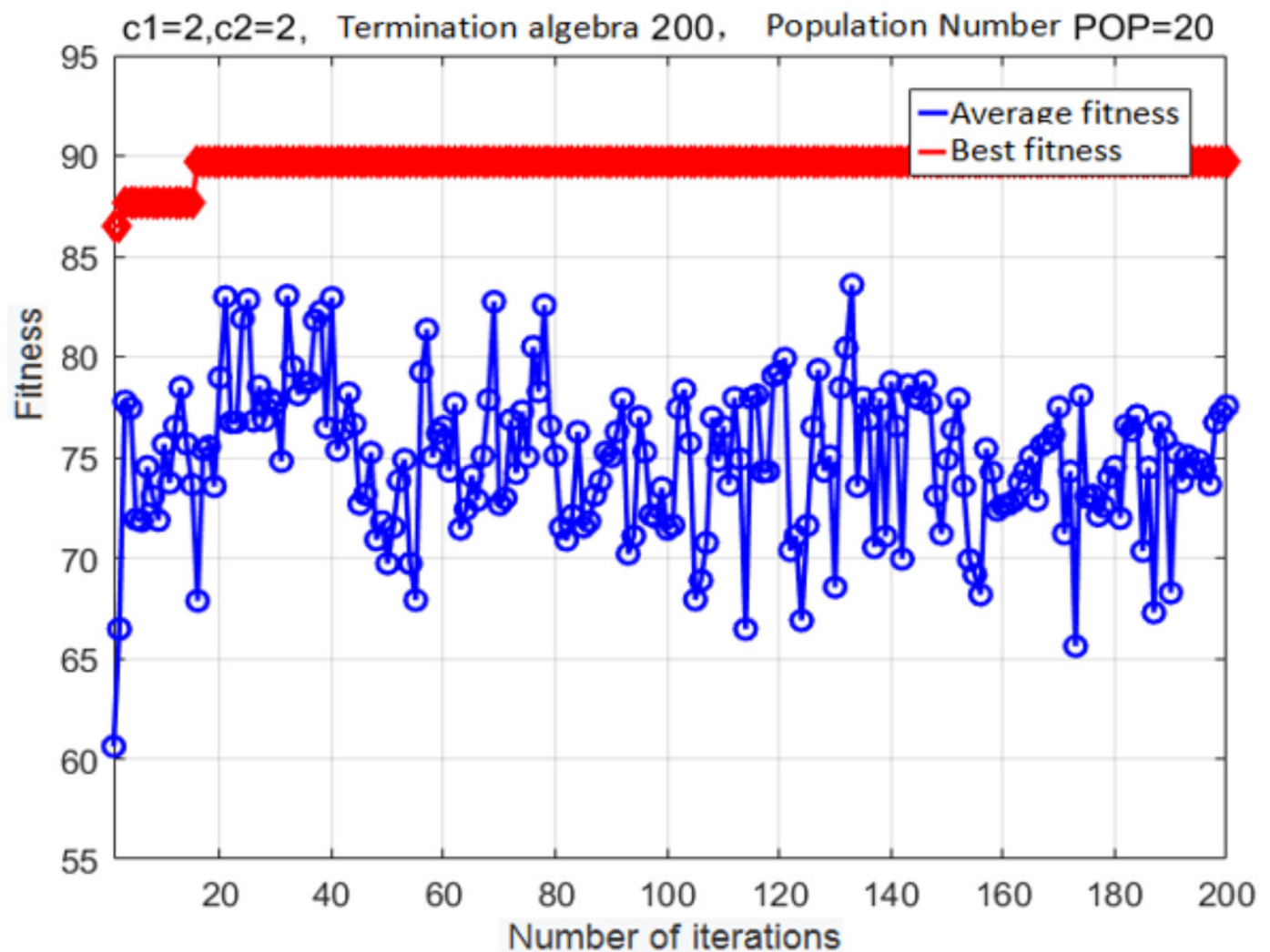
Figure 10

Fitness curve obtained after the variant PSO.
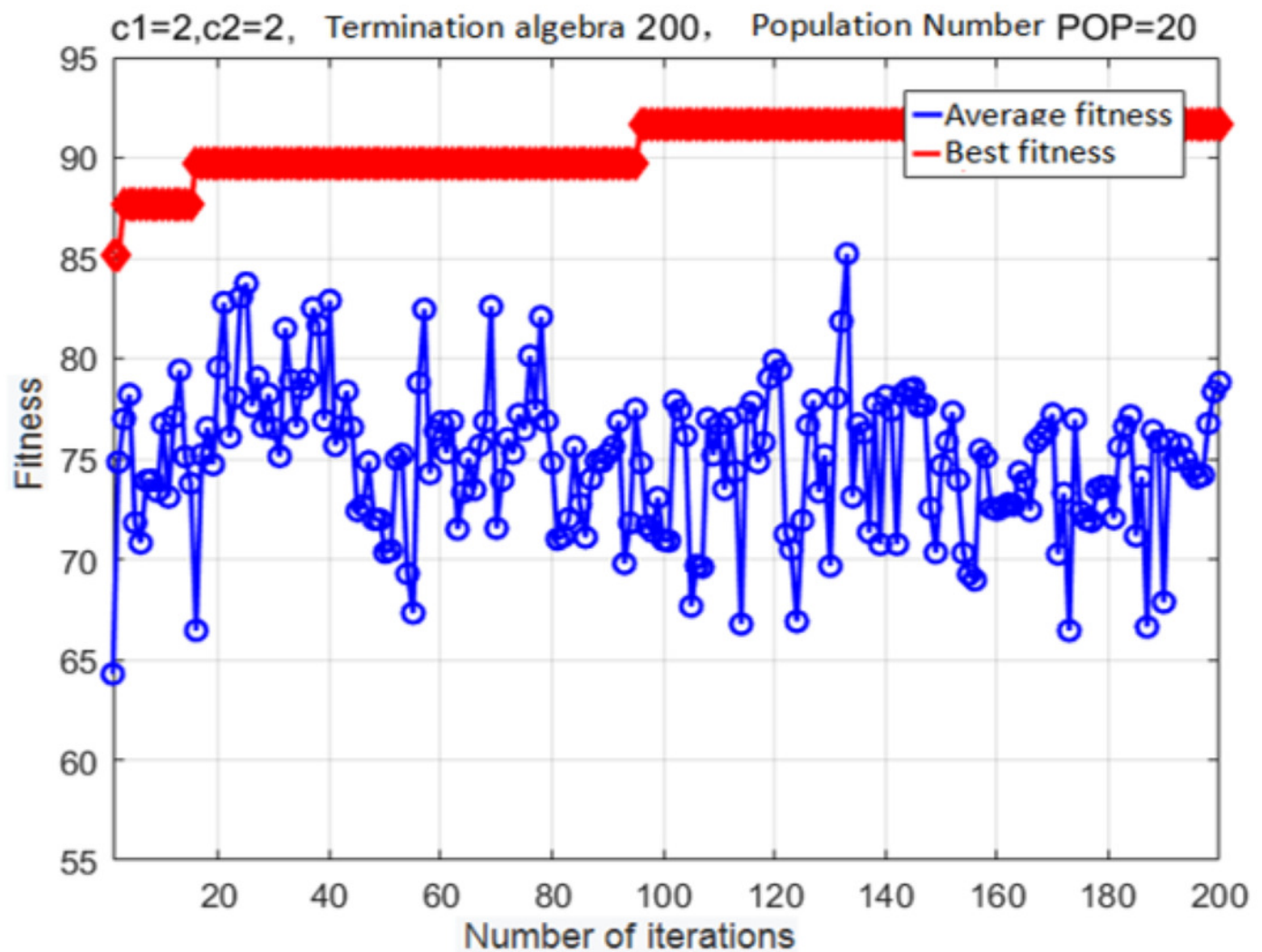
Figure 11

Validation results of the SVM model, for conventional PSO.
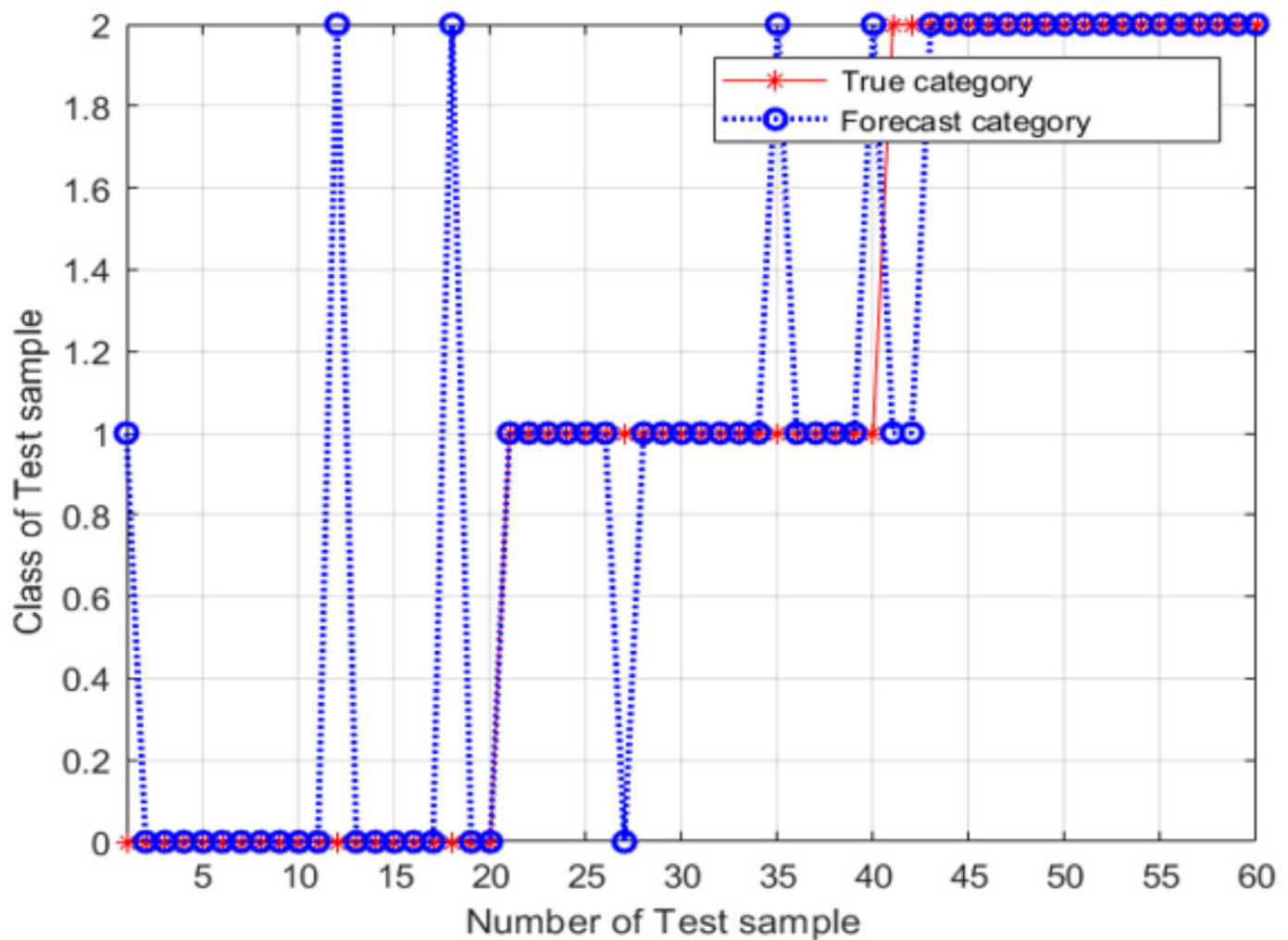
Figure 12

Validation results of the SVM model, for variant PSO.